Liu, L.; Lopez-Haro, M.; Wittee Lopes, C.; Meira, DM.; Concepción Heydorn, P.; Calvino, JJ.; Corma Canós, A. (2020). Atomic-level understanding on the evolution behavior of subnanometric Pt and Sn species during high-temperature treatments for generation of dense PtSn clusters in zeolites. Journal of Catalysis. 391:11-24. https://doi.org/10.1016/j.jcat.2020.07.035

Atomic-Level Understanding on the Evolution Behavior of Subnanometric Pt and Sn Species during High-Temperature Treatments for Generation of Dense PtSn Clusters in Zeolites

Lichen Liu,[1] Miguel Lopez-Haro,[2] Christian W. Lopes,[1] Debora M. Meira,[3†] Patricia Concepcion,[1] Jose J. Calvino[2] and Avelino Corma[1]*

[1] *Instituto de Tecnología Química, Universitat Politècnica de València-Consejo Superior de Investigaciones Científicas, Av. de los Naranjos s/n, Valencia 46022, Spain*

[2] *Departamento de Ciencia de los Materiales e Ingeniería Metalúrgica y Química Inorgánica, Facultad de Ciencias, Universidad de Cádiz, Cádiz, Spain*

[3] *European Synchrotron Radiation Facility, 6 Rue Jules Horowitz, Grenoble, BP 156, F-38042, France*

*Corresponding author. Email: acorma@itq.upv.es

†present address: CLS@APS sector 20, Advanced Photon Source, Argonne National Laboratory, 9700 S. Cass Avenue, Argonne, IL 60439, USA

Abstract

To achieve high-loading of stable subnanometric metal clusters on solid carriers is a challenge since those small metal clusters have strong tendency to sinter into larger nanoparticles. Development of facile synthesis methodologies to obtain subnanometric metal catalysts with high metal loading and high stability against sintering at high temperature (>500 ^{o}C) in reductive atmosphere (such as H_2) is critical for the practical applications. In this work, we will present and discuss the generation of high-loading (~1.4 wt%) subnanometric Pt clusters confined in the sinusoidal channels of MFI zeolite, on the basis of the atomic-level understanding on the evolution of Pt and Sn species during high-temperature oxidation-reduction treatments. It will be shown that the structural evolution of Pt and Sn species is dependent on the post-synthesis treatments. The Pt particles on the external surface can disintegrate into subnanometric Pt species and get stabilized in the zeolite channels during high-temperature calcination in air while Sn species migrate from surface region to internal region during high-temperature reduction treatment at 650 ^{o}C. The resultant material containing bimetallic PtSn clusters confined in the 10MR sinusoidal channels of the purely siliceous MFI zeolite show excellent catalytic activity and stability, as demonstrated for dehydrogenation of light alkanes at high reaction temperature.

Keywords

Metal clusters, Isolated atoms, Pt, MFI zeolite, Propane dehydrogenation, Structural evolution

Graphic Abstract

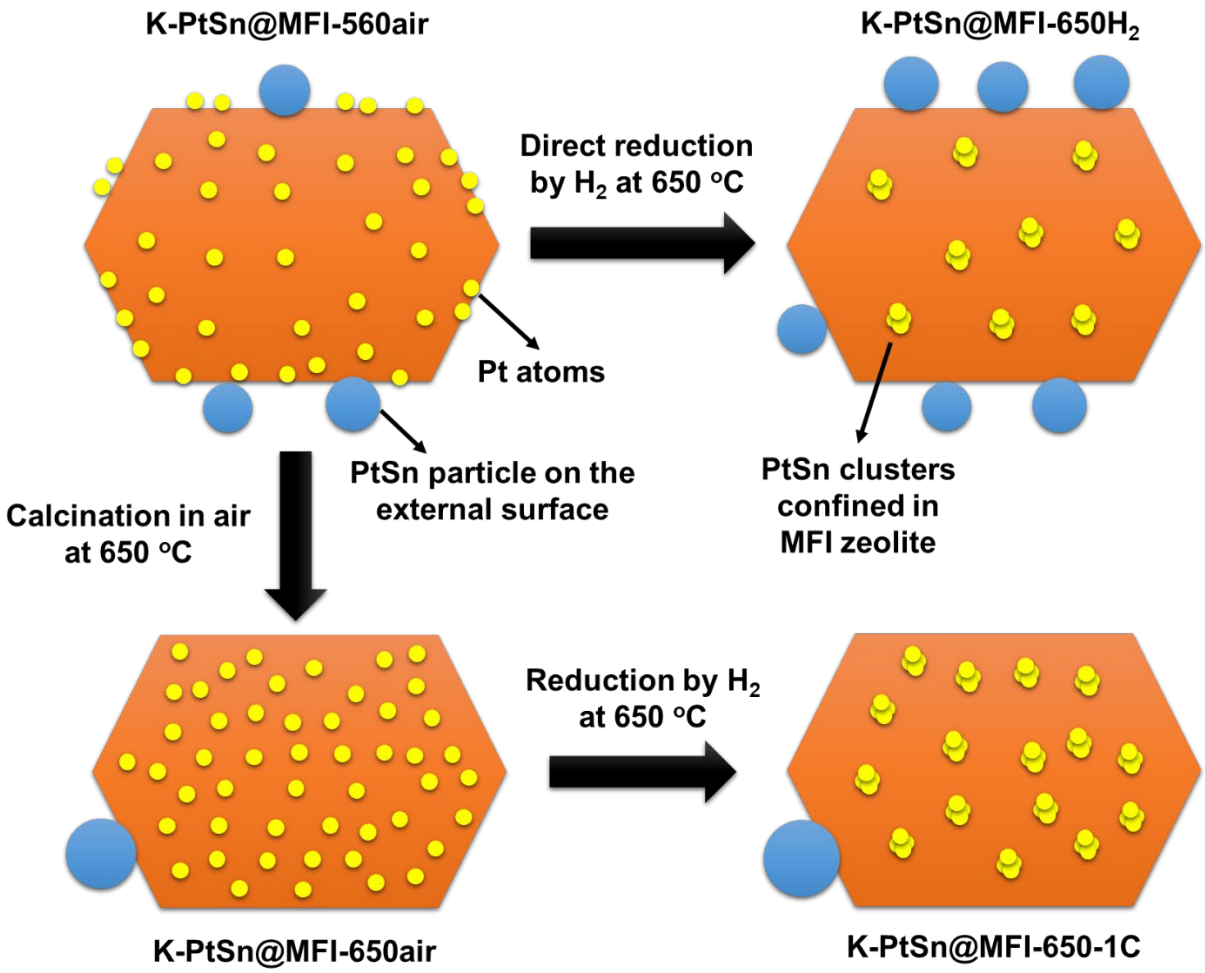

Highlights

- High-loading PtSn bimetallic clusters are encapsulated in pure-silica MFI zeolite
- Pt and Sn species show dynamic structural evolution during redox treatment
- The evolution behavior has been followed by AC-STEM at atomic level
- The bimetallic PtSn clusters show high stability against sintering up to 650 °C
- The optimized PtSn clusters show excellent reactivity for propane dehydrogenation

1. Introduction

Tremendous attention has been drawn in recent years to the subnanometric metal catalysts in the heterogeneous catalysis community and new catalytic behaviors have been reported with those metal entities [1-4]. However, to translate those fundamental findings into practical applications, synthesis methodologies for the generation of subnanometric metal catalysts with high stability and scalable production should be developed [5-7].

It has been reported in the literature that, single atoms or metal clusters can be feasibly generated on various solid carriers with a high metal loading. Single Pt atoms with total Pt loading above 1 wt% can be generated on metal oxides such as CeO_2 and Fe_2O_3 by conventional impregnation or co-precipitation, followed by calcination in air [8,9]. However, those Pt atoms will agglomerate into nanoparticles (>1 nm) after thermal annealing in N_2 or reduction treatment with H_2 or CO (even at 200-300 ºC) [10,11]. Therefore, it still remains challenging to stabilize subnanometric metal clusters after high-temperature reduction treatment (>500 ºC), especially for samples with metal loading above 1 wt%.

To achieve that goal, inorganic porous materials, such as zeolites, can be an ideal support to host and confine subnanometric metal species against sintering under harsh conditions. Indeed, it has been demonstrated that metal nanoparticles or subnanometric metal clusters can be encapsulated in zeolites, achieving high stability and shape-selective catalytic properties [12-17]. For instance, small metal nanoparticles such as Pt and Pd have been stabilized in various zeolites (CHA, MFI, BEA etc.) by introducing the metal precursor during the synthesis or through the interzeolite transformation and seed-directed synthesis [18-20]. However, the metal loading in those works are mostly below 1 wt%, while the metal entities can sinter into particles larger than 1 nm after being reduced by H_2 at higher temperature (≥600 ºC) and show irregular distributions in the zeolite crystallites.

The structural evolution of subnanometric metal species as a response to the change of the environment has been observed in numerous systems and various supported metal catalysts [21,22]. By advanced in situ/operando characterization techniques such as high-resolution TEM and X-ray absorption spectroscopy, we have gained knowledge on the behavior of the atomically dispersed metal species [23]. With respect to metal-zeolite materials, the dynamic structural transformations of metal species within the porous structures have also been studied by several spectroscopic techniques [15,24].

However, due to their complex structures and low stability under electron beam, quite limited results with atomic-level resolution have been reported on the evolution behavior of metal atoms and clusters confined in zeolites in the literature [25,26].

In this work, we will demonstrate the feasibility to obtain a pure-silica MFI zeolite containing subnanometric Pt (~1.4 wt%) and Sn species. The behavior of Pt and Sn species during high-temperature oxidation-reduction treatments will be studied at atomic level by STEM-iDPC imaging technique, which allows us to obtain information on the location and evolution of Pt atoms and clusters in the zeolite structure. This study evidences that Pt particles located on the external surface in the as-synthesized material disintegrate into subnanometric Pt species during high-temperature calcination in air, while Sn species migrate from the surface to the internal regions during high-temperature reduction treatments. With these insights at atomic level, we have prepared a K-PtSn@MFI material containing a large population of stable subnanometric bimetallic PtSn clusters confined in the 10MR sinusoidal channels of MFI zeolite structure by combining one-pot synthesis and post-synthesis treatments. The materials prepared by this procedure are highly stable and active catalyst for propane dehydrogenation reaction at high temperature.

2. Experiments

2.1 One-pot synthesis of MFI zeolites with the encapsulation of Pt

2.1.1 Synthesis of K-free Pt@MFI

Pt nanoparticles encapsulated in MFI zeolite were prepared by a one-pot synthesis. Firstly, a tetrapropylammonium hydroxide (TPAOH) solution was prepared by mixing 8.12 g of K-free TPAOH solution (40 wt%, from Alfa-Aesar (product code: 17456.22) and 20.1 g of distilled water at room temperature. Then, 8.24 g Tetraethyl orthosilicate (TEOS) was hydrolyzed with tetrapropylammonium hydroxide solution (TPAOH) at room temperature for 6 h under stirring (500 rpm). The resultant solution was divided into two parts with the same weight. To each portion of the solution, 233 μL H_2PtCl_6 aqueous (0.38 mol/L) and 150 μL of ethylenediamine were added while stirring was kept for 20 min. The resultant yellow solution was then transferred to Teflon-lined autoclaves and heated in an electric oven at 175 ºC for 96 h under static conditions. The amount of Pt in the final Pt@MFI material is 1.4 wt%. After the hydrothermal process, the solid product was isolated by filtration and washed

with distilled water and acetone and then dried at 60 ºC. Then the solid sample was calcined under an air flow at 560 ºC for 8 h.

2.1.2 Synthesis of K-free PtSn@MFI

PtSn nanoparticles encapsulated in MFI zeolite were prepared by a similar one-pot synthesis as the Pt@MFI sample. Additionally, 50 mg of $SnCl_4 \cdot 5H_2O$ was added to the mixture of TEOS-TPAOH-water together with 233 μL H_2PtCl_6 aqueous (0.38 mol/L) and 150 μL of ethylenediamine under rigorous stirring. The amount of Pt and Sn in the final PtSn@MFI material is 1.4 wt% and 0.7 wt%, respectively.

2.1.3 Synthesis of K-Pt@MFI

K-promoted Pt clusters encapsulated in MFI zeolite were prepared by a one-pot synthesis. Firstly, a tetrapropylammonium hydroxide (TPAOH) solution was prepared by mixing 5.0 g of K-free TPAOH solution (40 wt%, from Alfa-Aesar, product code: 17456.22) and 6.24 g of TPAOH solution (20 wt%, from Sigma-Aldrich containing ~0.6 wt% of K, product code: 254533-100G) and 17.0 g of distilled water at room temperature. Then, 8.24 g Tetraethyl orthosilicate (TEOS) were hydrolyzed with tetrapropylammonium hydroxide solution (TPAOH) at room temperature for 6 h under stirring (500 rpm). The resultant solution was divided into two parts with the same weight. To each portion of the solution, 233 μL of H_2PtCl_6 aqueous (0.38 mol/L) and 150 μL of ethylenediamine were added and stirring was kept for 20 min. The resultant yellow solution was then transferred to Teflon-lined autoclaves and heated in an electric oven at 175 ºC for 96 h under static conditions. The amounts of Pt and K in the final product were 1.4 wt% and 0.7 wt%, respectively. After the hydrothermal process, the solid product was isolated by filtration and washed with distilled water and acetone and then dried at 60 ºC. Then the solid sample was calcined under air flow at 560 ºC for 8 h.

2.1.4 Synthesis of K-PtSn@MFI

K-promoted PtSn clusters encapsulated in MFI zeolite were prepared by a similar one-pot synthesis as the K-Pt@MFI sample. Additionally, 50 mg of $SnCl_4 \cdot 5H_2O$ was added to the mixture of TEOS-TPAOH-water together with 233 μL H_2PtCl_6 aqueous (0.38 mol/L) and 150 μL of ethylenediamine

under rigorous stirring. The amounts of Pt, K and Sn in the final product were 1.4 wt%, 0.7 wt% and 0.6 wt%, respectively.

2.1.5 Synthesis of K-PtSn/MFI-imp by conventional incipient wetness impregnation.

Firstly, a K-promoted purely siliceous MFI support was prepared by following the procedure for the K-Pt@MFI sample without the addition of Pt precursor. After the hydrothermal synthesis, the solid product was recovered and then calcined in air at 560 ºC for 8 h. Taking that K-MFI as support, Pt and Sn together with ethylenediamine is introduced to the K-MFI support by conventional incipient wetness impregnation. The amount of Pt and Sn is the same to the K-PtSn@MFI sample prepared by one-pot synthesis.

2.1.6 High-temperature redox treatment with the K-PtSn@MFI sample

To promote the redispersion of Pt species in MFI zeolite, we have carried out a high temperature oxidation-reduction treatment at 650 ºC. For one cycle of redox treatment, the K-PtSn@MFI sample was oxidized by calcination in air at 650 ºC for 3 h. After that, the oxidized sample was reduced by H_2 at 650 ºC for 3 h. Consecutive cycles of redox treatments were carried out to stepwisely improve the dispersion of Pt species in MFI crystallites.

2.2 Characterization

Powder X-ray diffraction (XRD) was performed with a HTPhilips X'Pert MPD diffractometer equipped with a PW3050 goniometer using Cu Kα radiation and a multisampling handler.

The amounts of silanol groups in the Pt-zeolite materials were measured by FT-IR. Before the measurement, the Pt-zeolite materials were dehydrated in vacuum at 400 ºC and then cool to room temperature in the vacuum IR cell. The IR spectra of the Pt-zeolite were then recorded by a Nicolet 710 FT-IR spectrometer.

Samples for electron microscopy studies were prepared by dropping the suspension of the solid samples in CH_2Cl_2 directly onto holey-carbon coated copper grids. Electron Microscopy measurements were performed using two types of microscopes. Thus, non-corrected JEOL 2100F microscope operating at 200 kV both in transmission (TEM) and scanning-transmission modes (STEM)

was used to record High Angle Annular Dark Field (HAADF), Z-contrast, images at low resolution. High resolution HAADF-STEM and STEM-iDPC imaging was performed on a double aberration corrected (AC), monochromated, FEI Titan^3 Themis 60-300 microscope working at 300 kV. More details on the measurements are described in the supporting information.

IR spectra of adsorbed CO on Pt-zeolite samples were recorded at room temperature with a Nexus 8700 FTIR spectrometer using a DTGS detector and acquiring at 4 cm^{-1} resolution. An IR cell allowing in situ treatments in controlled atmospheres and temperatures from 25 °C to 500 °C has been connected to a vacuum system with gas dosing facility. For IR studies the samples were pressed into self-supported wafers and pre-treated in H_2 flow at 450 °C for 2 h followed by vacuum treatment (10^{-5} mbar). After activation the samples were cooled down to 25 °C under dynamic vacuum conditions followed by CO dosing at increasing pressure (0.4-8.5 mbar). IR spectra were recorded after each dosage of CO.

The last technique, iDPC (for Integrated-Differential Phase Contrast) imaging, provides in this microscope atomically resolved images in which the contrasts are roughly related to the atomic number of the elements under the beam in thin specimen, instead of the roughly Z^2-dependent contrasts obtained in HAADF-STEM images. By using a 4-segment detector, this technique allows imaging light elements, as it is the case of O, in the presence of heavier ones (Si, Z=14) under very low electron dose conditions, which is a key aspect in the atomic scale structural analysis of zeolites, which are very sensitive to electron beams. In particular, 2048 x 2048 HAADF-iDPC image pairs were recorded simultaneously using a convergence angle of 18.6 mrad and collection angles of 53-198 mrad. This configuration allowed us to optimize the collection of the signals on the HAADF and FEI DF4 detectors. In order to limit the damage by the electron beam, a fast image recording protocol was used by combining a beam current of 10-30 pA, a 1.25-2.5 µs dwell time (corresponding to dose rates of 2500-3900 $e^-/Å^2$) and an automated fine-tuning alignment of A1 and C1 using the OptiSTEM software.

To determine the spatial distribution of the metallic species within the zeolite framework, a specific methodology for the digital analysis of the experimental images has been developed and coded in a home-made MATLAB script. First, to improve the signal-to-noise, the HR-HAADF STEM images were denoised by combining the Anscomb transform and Undecimated Wavelet Transforms (UWVT) [27]. Then, a user-independent, fully automated, segmentation of image contrasts by clustering

techniques (K-means method) was applied to recognize and classify the metallic entities, which is a requirement to guarantee statistically meaningful and unbiased results.

The STEM-EDS measurements were performed on the JEOL-2100F microscope equipped with a X-MAX silicon drift detector supplied by Oxford Instruments. The quantification of EDS results was performed with the AZtecTEM software. The following five elements, line types and the corresponding k factors were considered in the quantification procedure: O-K (2.02), Si-K (1.00), K-K (1.009), Sn-L (1.924) and Pt-M (1.726).

X-ray absorption experiments at the Pt (11564 eV) L_{III} and Sn (29200 eV) K-edges, were performed at the BL22 (CLÆSS) beamline of ALBA synchrotron (Cerdanyolla del Vallès, Spain) [28] and beamline of BM23 in ESRF synchrotron (Grenoble, France) [29]. The white beam was monochromatized using a Si (111) and (311) double crystals, respectively; harmonic rejection has been performed using Rh-coated silicon mirrors. The spectra were collected in transmission (Pt L_{III}-edge) and fluorescence (Sn K-edge) modes by means of the ionization chambers filled with appropriate gases (Pt L_{III}-edge: 95 % N_2 + 5 % Kr for I_0 and 17.1 % N_2 + 82.9 % Kr for I_1; Sn K-edge: 89.4 % N_2 + 10.6 % Kr for I_0 and 100 % Kr for I_1) and a fluorescence solid-state detector. Samples in the form of self-supported pellets of optimized thickness have been located inside an in-house built multipurpose cell allowing *in situ* experiments. Several scans were acquired at each measurement step to ensure spectral reproducibility and good signal-to-noise ratio. The data reduction and extraction of the $\chi(k)$ function has been performed using Athena code. EXAFS data analysis has been performed using the Arthemis software [30]. Phase and amplitudes have been calculated by FEFF6 code [30]. The values of E_0 (inflection point in the first derivative of XANES spectra) used for data alignment were the following: 29200 eV for Sn metal, 29201 eV for SnO, 29204 eV for SnO_2 and 11564 eV for Pt metal.

2.3 Catalytic studies of Pt-zeolite materials for propane dehydrogenation reactions.

The dehydrogenation of propane to propylene was chosen as model reaction to test the reactivity and stability of Pt particles or clusters encapsulated in pure-silica MFI zeolite. The reaction was performed with a fix-bed reactor under atmospheric pressure using N_2/propane as feed gas at 600 ºC. The products were analyzed by a GC which can detect cracking products (methane, ethene and ethane), propylene, C4, C5 and aromatics. Before reaction, the catalyst was reduced by H_2 flow (35 mL/min)

at 600 ºC for 1 h with a ramp rate of 10 ºC/min from room temperature up to 600 ºC. After the reduction pre-treatment, the atmosphere was changed to reaction feed gas (5 mL/min of propane and 16 mL/min of N_2 as balanced gas). After the propane dehydrogenation test, the sample was cooled down to ~100 ºC and started to be regenerated by calcination in air at 600 ºC for 2 h with a ramp rate of 10 ºC/min from ~100 ºC up to 600 ºC. After calcination in air, the sample was cooled down to ~100 ºC again and then reduced by H_2 at 600 ºC for 1 h ~100 ºC up to 600 ºC before the second cycle for propane dehydrogenation reaction. After the second cycle of propane dehydrogenation test, the sample was cooled down to ~100 ºC and started to be regenerated by calcination in air at 600 ºC for 2 h with a ramp rate of 10 ºC/min from ~100 ºC up to 600 ºC. After calcination in air, the sample was cooled down to ~100 ºC again and then reduced by H_2 at 600 ºC for 1 h ~100 ºC up to 600 ºC before the third cycle for propane dehydrogenation reaction.

3. Results and Discussion

First of all, we have found that, when conveniently adapted, our synthesis method can allow the generation of high-loading of Pt species (~1.4 wt%, more than 3 times of the Pt loading in our previous work) in the form of subnanometric metal clusters within pure-siliceous MFI zeolite crystallites (see **experimental section** for synthesis details) [31]. As discussed in the **supporting information** (**Fig. S1-S37**), the various Pt-MFI zeolite samples (K-free Pt@MFI, PtSn@MFI, K-Pt@MFI, K-PtSn@MFI, Na-Pt@MFI and Cs-Pt@MFI) prepared here with higher Pt loading are of practically the same quality as the materials with low Pt loading (~0.4 wt%) studied in our previous work, indicating the robustness of our synthesis method. The size distributions of Pt particles are greatly dependent on the chemical compositions. According to the characterization results, the K-PtSn@MFI sample with both alkaline metals (K) and a second metal promoter (Sn) shows the highest percentage of subnanometric Pt clusters confined in the 10MR sinusoidal channels after calcination in air at 560 ºC and subsequent reduction in H_2 at 600 ºC. The catalytic performance for propane dehydrogenation reaction also indicate the important roles of K and Sn on stabilization and reactivity modulation of Pt clusters.

However, due to the high Pt loading and non-uniform distribution of Pt in the material, some Pt nanoparticles are formed on the surface or subsurface of MFI zeolite crystallites in the K-PtSn@MFI sample (see **Fig. 1**). Considering the heterogeneous distribution of Pt species in the high-loading K-

PtSn@MFI materials, we have combined here the one-pot synthesis with post-synthesis treatments to achieve our final goal of obtaining a uniform distribution of highly stable subnanometric Pt clusters within the pores of the zeolite crystallites. In this work, we will present a systematic study on how the spatial distribution of Pt species in zeolite crystallites is modified during the post-synthesis treatments and its impact on catalytic performance.

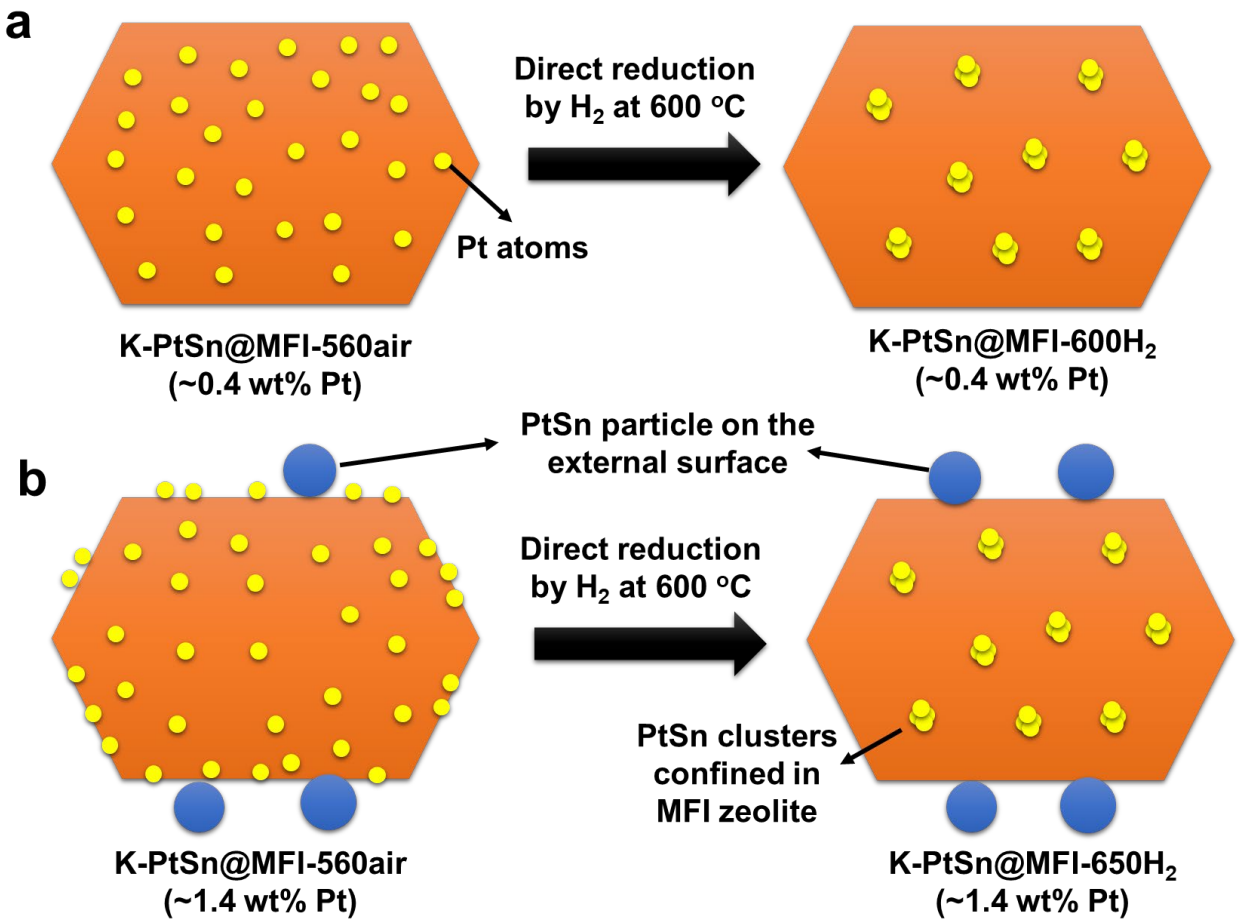

Fig. 1. Schematic illustration on the K-PtSn@MFI samples with different Pt loadings prepared by one-pot synthesis. When increasing the Pt loading from ~0.4 wt% to ~1.4 wt%, some Pt nanoparticles will form on the external surface of MFI zeolite crystallites after reduction by H_2 at 600 °C.

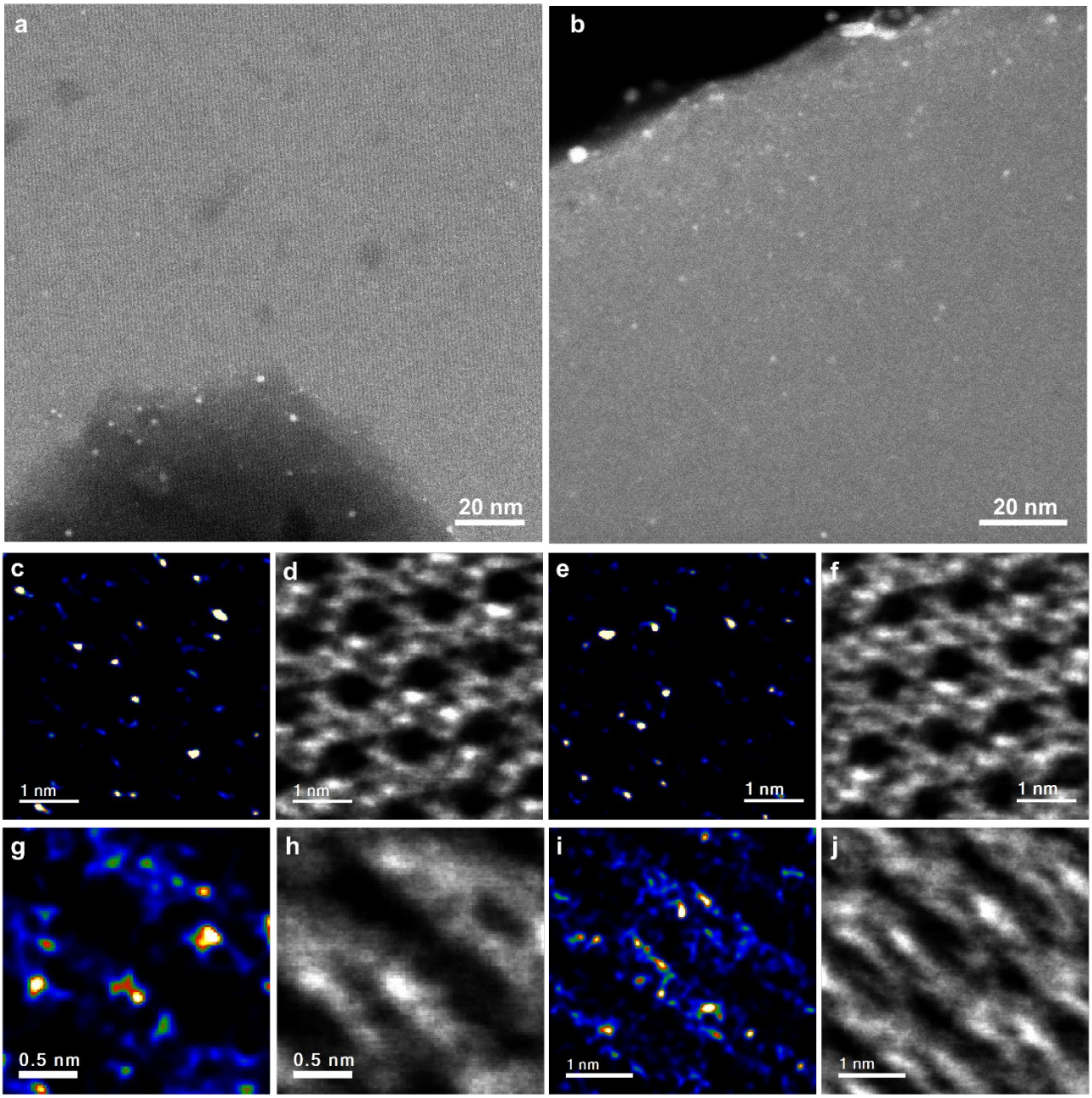

Fig. 2. Structural characterizations of K-PtSn@MFI-560air sample obtained after hydrothermal synthesis and subsequent calcination in air at 560 ºC. (a, b) Low-magnification STEM images of the K-PtSn@MFI-560air sample, showing the presence of Pt nanoparticles on the external surface of MFI zeolite crystallites. (c-j) Identification of the position of isolated Pt atoms in the MFI zeolite structure by the combination of HAADF-STEM and iDPC imaging technique. High-resolution HAADF-STEM (c, e, g, i) and their corresponding iDPC images (d, f, h, j) of K-PtSn@MFI-560air sample, showing the presence of isolated Pt atoms in MFI zeolite. By correlating the HR HAADF-STEM images and iDPC images, the location of Pt atoms can be determined to be in the 10MR sinusoidal channels.

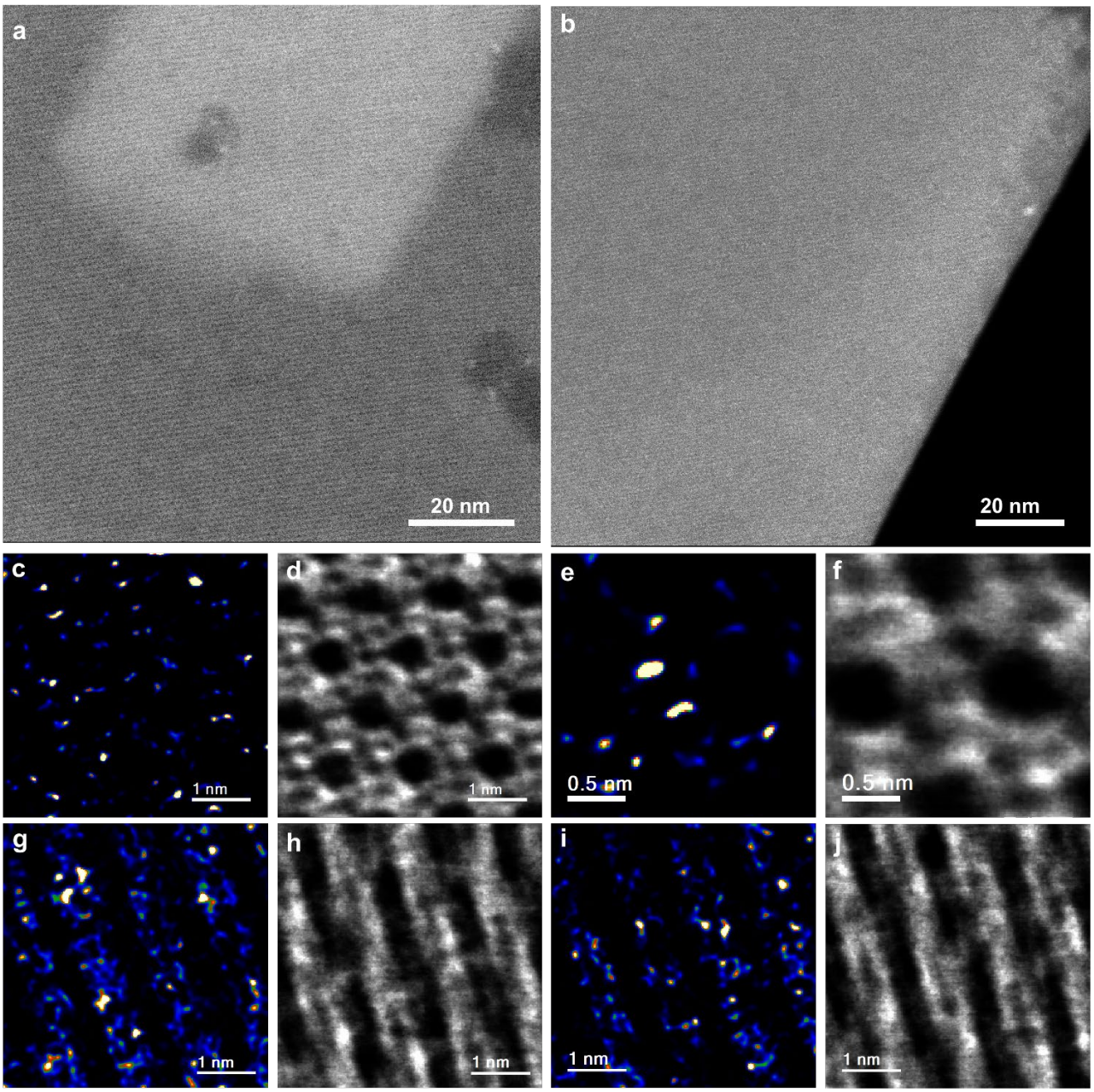

Fig. 3. Structural characterizations of K-PtSn@MFI-650air sample obtained after an additional calcination treatment with the pristine K-PtSn@MFI-560air sample in air at 650 ºC. (a, b) Low-magnification STEM images of the K-PtSn@MFI-650air sample, showing the presence of a very few Pt nanoparticles on the external surface of MFI zeolite crystallites. The number of Pt nanoparticles is much lower than that in the K-PtSn@MFI-560air sample, implying the redispersion of Pt nanoparticles during calcination at higher temperature. (c-j) Identification of the position of isolated Pt atoms in the MFI zeolite structure by the combination of HAADF-STEM and iDPC imaging technique. High-resolution HAADF-STEM (c, e, g, i) and their corresponding iDPC images (d, f, h, j) of K-PtSn@MFI-560air sample, showing the presence of isolated Pt atoms in MFI zeolite. By correlating the HR HAADF-STEM images and iDPC images, the location of Pt atoms can be determined to be in the 10MR sinusoidal channels.

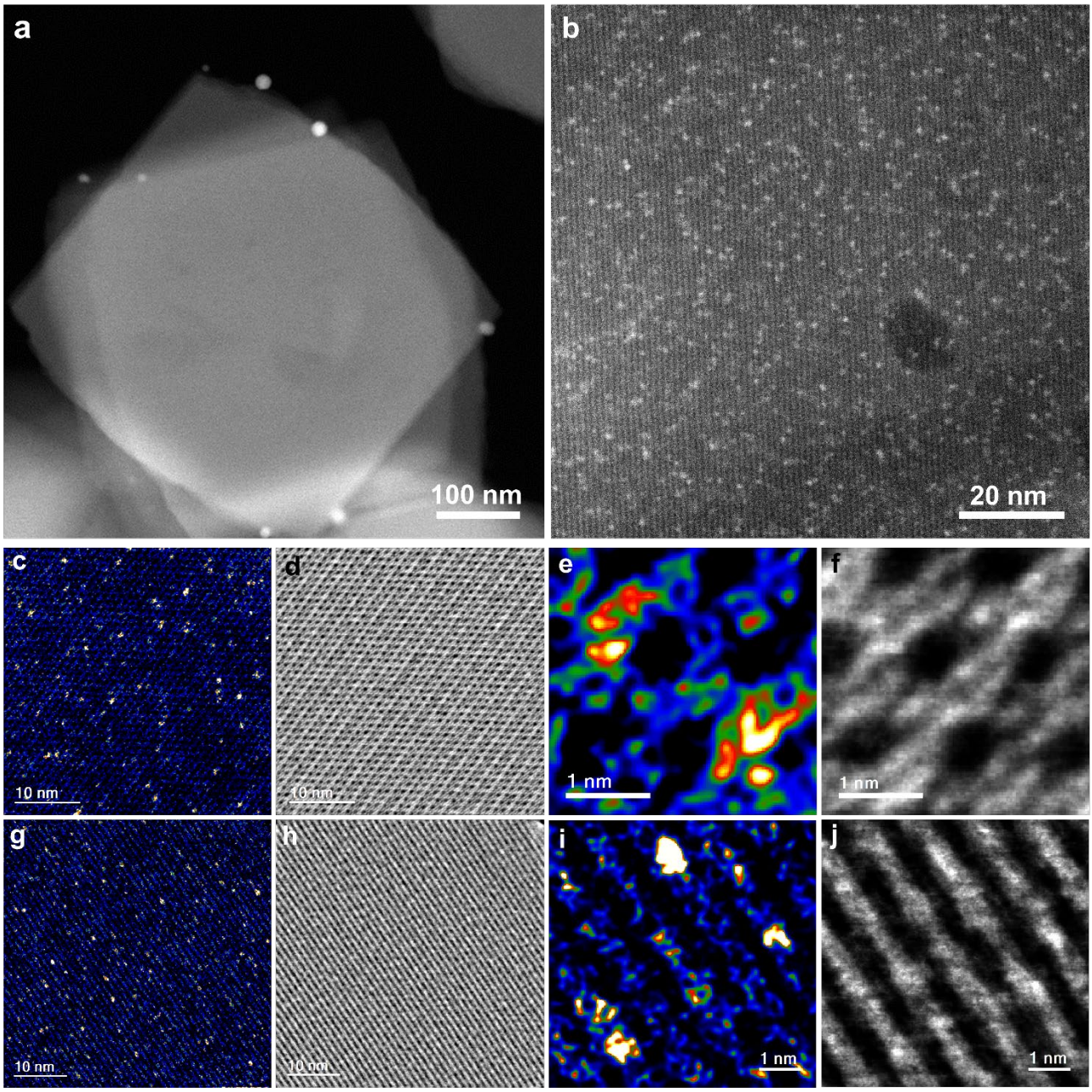

Fig. 4. Structural characterizations of K-PtSn@MFI-650-1C sample obtained after one cycle of calcination and reduction treatment on the pristine K-PtSn@MFI-560air sample at 650 ºC. (a) A few Pt nanoparticles can be observed on the external surface of K-PtSn@MFI zeolite crystallites. (b) Meantime, subnanometric Pt clusters with very good dispersion can be observed in the MFI zeolite structure. (c-j) Identification of the position of subnanometric Pt clusters in the MFI zeolite structure by the combination of HAADF-STEM and iDPC imaging technique. High-resolution HAADF-STEM (c, e, g, i) and their corresponding iDPC images (d, f, h, j) of K-PtSn@MFI-650-1C sample, showing the presence of subnanometric Pt species in MFI zeolite and their location on the zeolite structure. By correlating the HR HAADF-STEM images and iDPC images, the location of Pt clusters can be determined to be in the 10MR sinusoidal channels.

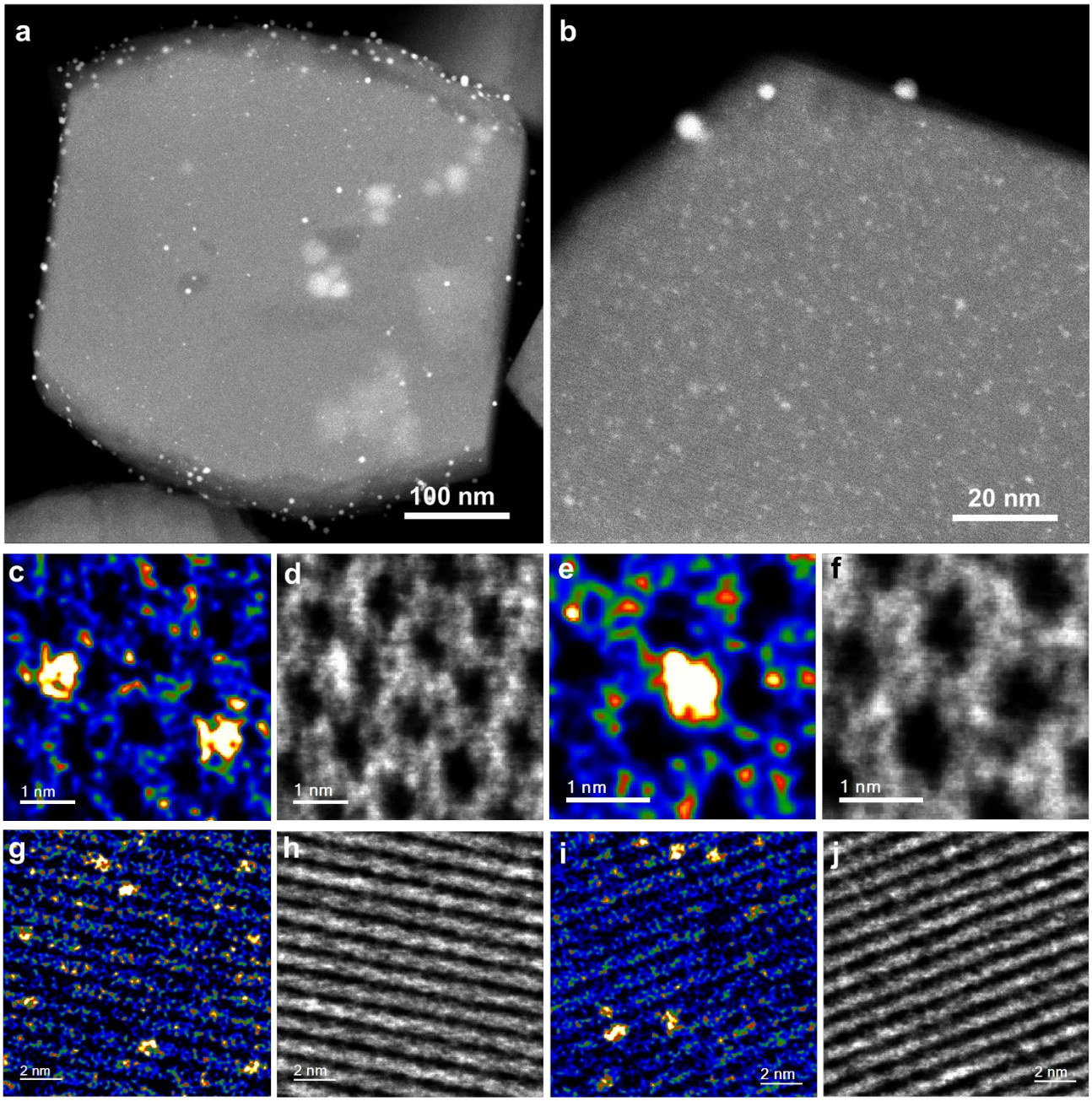

Fig. 5. Structural characterizations of K-PtSn@MFI-650H_2 sample obtained after direct reduction treatment by H_2 on the pristine K-PtSn@MFI-560air sample at 650 ºC. (a) A large number of Pt nanoparticles can be observed on the external surface of K-PtSn@MFI zeolite crystallites, which is much higher than the pristine K-PtSn@MFI-560air and the K-PtSn@MFI-650-1C sample. (b) Meantime, subnanometric Pt clusters can also be observed in the MFI zeolite structure. (c-j) Identification of the position of subnanometric Pt clusters in the MFI zeolite structure by the combination of HAADF-STEM and iDPC imaging technique. High-resolution HAADF-STEM (c, e, g, i) and their corresponding iDPC images (d, f, h, j) of K-PtSn@MFI-650H_2 sample, showing the presence of subnanometric Pt species in MFI zeolite and their location on the zeolite structure. By correlating the HR HAADF-STEM images and iDPC images, the location of Pt clusters can be determined to be in the 10MR sinusoidal channels.

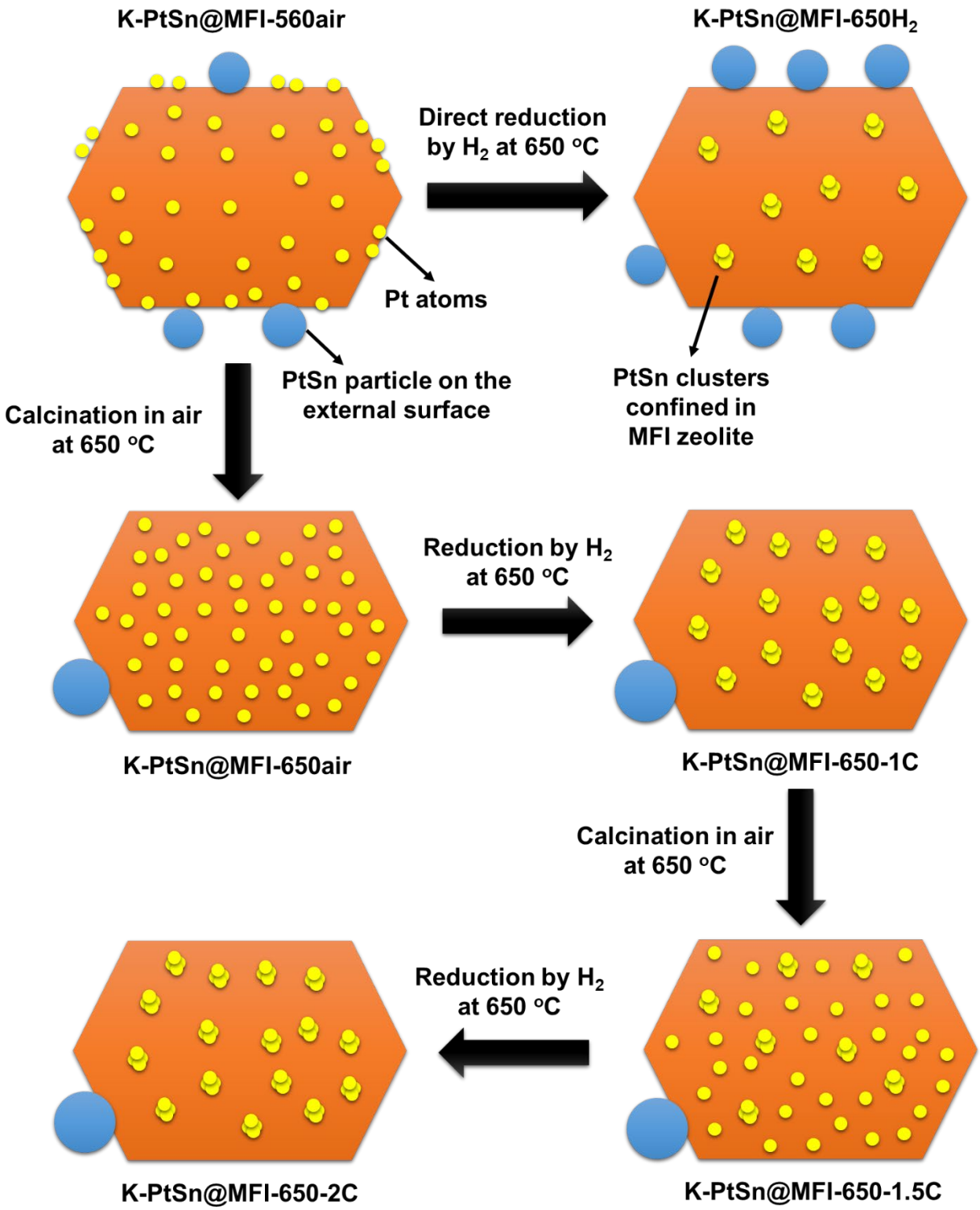

Fig. 6. Schematic illustration on the evolution of Pt species during high-temperature oxidation and reduction treatments. Direct reduction at 650 °C will cause the formation of many Pt nanoparticles on the external surface of MFI zeolite. After oxidation-reduction treatment, Pt nanoparticles on the external surface will migrate into the internal space and subsequently stabilized as Pt clusters in the sinusoidal channels.

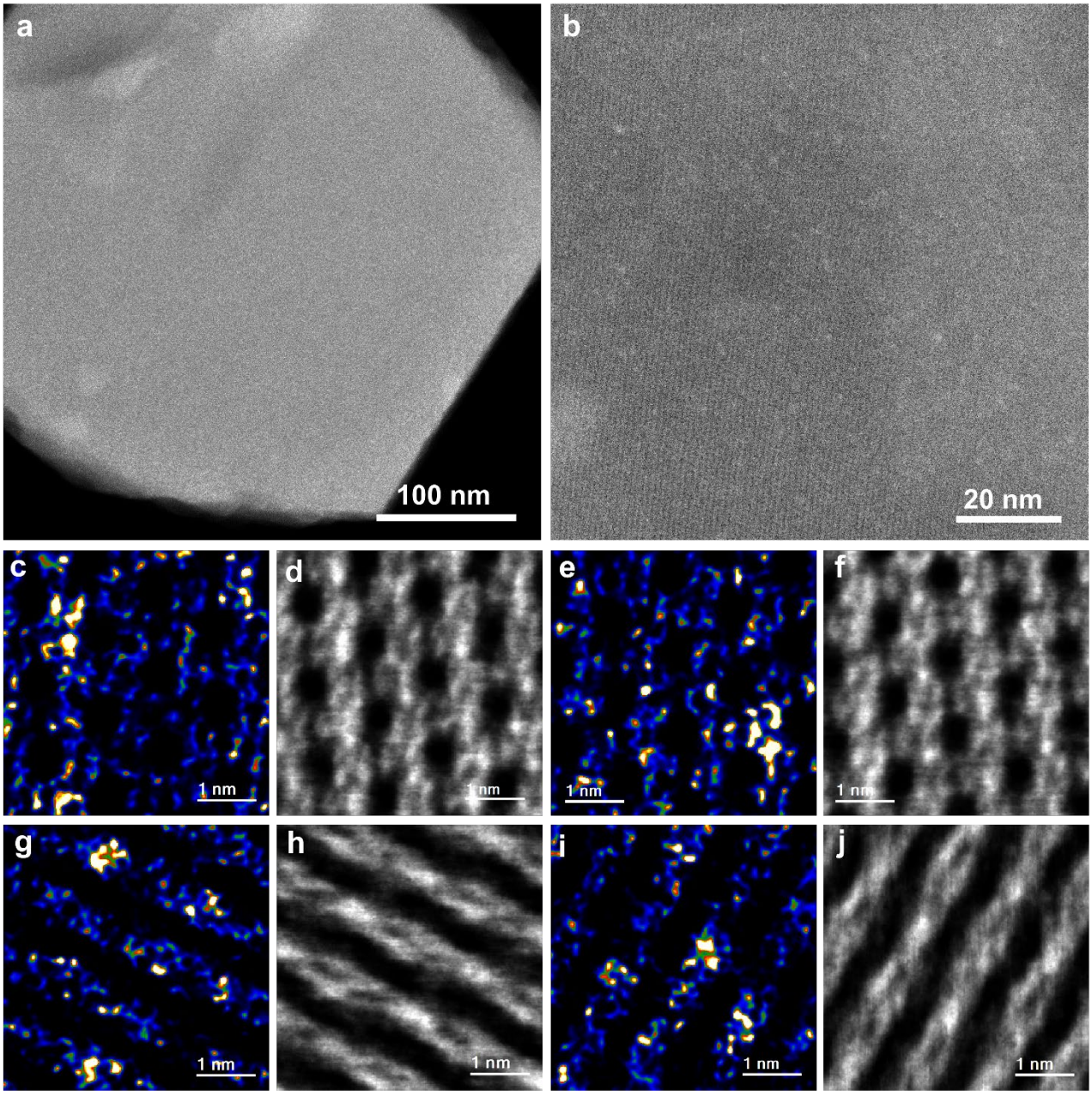

Fig. 7. Structural characterizations of K-PtSn@MFI-650-1.5C sample obtained after one calcination treatment on the K-PtSn@MFI-650-1C sample in air at 650 ºC. (a) Pt nanoparticles can be barely observed on the external surface of K-PtSn@MFI zeolite crystallites. (b) Meantime, some subnanometric Pt clusters and isolated Pt atoms can be observed in the MFI zeolite structure. (c-j) Identification of the position of subnanometric Pt clusters and isolated Pt atoms in the MFI zeolite structure by the combination of HAADF-STEM and iDPC imaging technique. High-resolution HAADF-STEM (c, e, g, i) and their corresponding iDPC images (d, f, h, j) of K-PtSn@MFI-650-1.5C sample, showing the presence of subnanometric Pt species in MFI zeolite and their location on the zeolite structure. By correlating the HR HAADF-STEM images and iDPC images, the location of Pt atoms and clusters can be determined to be in the 10MR sinusoidal channels.

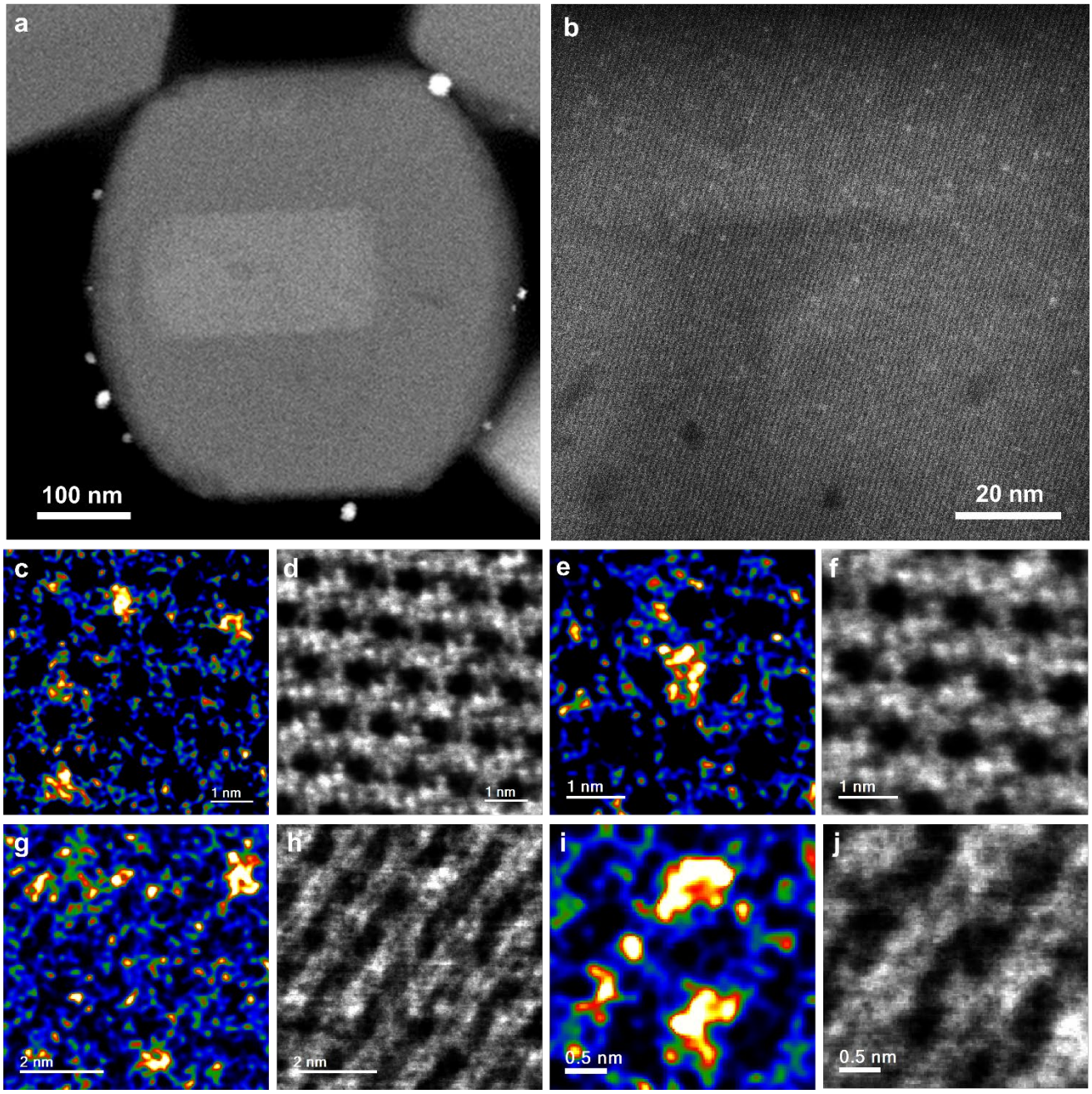

Fig. 8. Structural characterizations of K-PtSn@MFI-650-2C sample obtained after two cycles of calcination and reduction treatment on the pristine K-PtSn@MFI-560air sample at 650 ºC. (a, b) A very few Pt nanoparticles and subnanometric Pt clusters with very good dispersion can be observed in the MFI zeolite structure. (c-j) Identification of the position of subnanometric Pt clusters in the MFI zeolite structure by the combination of HAADF-STEM and iDPC imaging technique. High-resolution HAADF-STEM (c, e, g, i) and their corresponding iDPC images (d, f, h, j) of K-PtSn@MFI-650-2C sample, showing the presence of subnanometric Pt species in MFI zeolite and their location on the zeolite structure. By correlating the HR HAADF-STEM images and iDPC images, the location of Pt clusters can be determined to be in the 10MR sinusoidal channels.

To understand the location of subnanometric Pt species within the MFI structure for the high Pt loading samples and how those tiny species evolve during various treatments, we have characterized the K-PtSn@MFI samples with the newly developed method which involves the simultaneous use of STEM-HAADF and STEM-iDPC techniques. As shown in **Fig. 2**, in the initial K-PtSn@MFI sample obtained after calcination in air (named as K-PtSn@MFI-560air), a few Pt nanoparticles are observed on the external surface of some MFI zeolite crystallites (**Fig. S38**). Meanwhile, the presence of atomically dispersed Pt species in the sinusoidal channels has been confirmed by the paired HAADF-STEM and iDPC images, as shown in **Fig. S39-S40**. Note that, due to their low contrast, atomically dispersed Sn species are extremely difficult to be detected in the HAADF-STEM images. After high-temperature calcination at 650 ºC, the number of Pt nanoparticles is dramatically decreased and a few tiny Pt particles or clusters are observed in the STEM images (see **Fig. 3**). Pt atoms within the 10MR sinusoidal channels can also be identified by the high-resolution HAADF-iDPC paired images (see **Fig. S41-S43**), suggesting that the calcination at 650 ºC in air doesn't promote a preferential location of Pt atoms in the zeolite structure. Effectively, although the vast majority of the isolated Pt atoms observed in the K-PtSn@MFI-650air are located in the 10MR sinusoidal channels, a fraction of Pt atoms could be found at the intersectional voids or straight channels, which may result from the migrated Pt species from external surface to internal space of MFI zeolite.

The above results indicate that redispersion of Pt particles (<5 nm) at the external surface of MFI crystallites may occur through the disintegration of Pt nanoparticles in oxidative atmosphere and subsequent migration from external surface into the pore mouths of the 10MR sinusoidal channels. After one cycle of oxidation-reduction treatment by H_2 at 650 ºC (named as K-PtSn@MFI-650-1C), the atomically dispersed Pt species in the K-PtSn@MFI-650air sample will agglomerate and form Pt clusters of 0.5-0.6 nm confined in the 10MR sinusoidal channels, as visualized in the HAADF-STEM images (see **Fig. 4**), though a few Pt nanoparticles can be observed on the external surface of the zeolite crystallites. Interestingly, the location of subnanometric PtSn clusters in the K-PtSn@MFI-650-1C sample is preserved to be in the sinusoidal channels (see **Fig. S44-46**), indicating that the preferential location of the PtSn clusters in MFI zeolite is not affected by the high-temperature treatments. On the other hand, these results also confirmed that, the Pt atoms observed in the K-PtSn@MFI-650air sample should mainly locate in the 10MR sinusoidal channels.

For comparison, the K-PtSn@MFI-560air sample has been reduced by H_2 at 650 ºC (named as K-PtSn@MFI-650H_2). As shown in **Fig. 5**, a large number of Pt nanoparticles (2-10 nm) are formed on the external surface of MFI crystallites, though subnanometric PtSn clusters are also present (see more images in **Fig. S47-S50**). These results confirm the significant influence of the high-temperature calcination treatment on the spatial distribution of Pt species, which is a key step to generate dense subnanometric PtSn clusters in the zeolite crystallites.

The redispersion of Pt particles in zeolites, or generally on solid carriers, has already been observed during thermal treatments in the literature [15,32,33]. However, the position of Pt atoms or particles has not been fully revealed at atomic level in those prior works. According to the results presented above, we are able to describe the structural transformation behavior of subnanometric Pt species during the high-temperature redox treatments. As depicted in **Fig. 6**, part of the Pt species at the surface or subsurface can diffuse to the internal space of the MFI crystallite during the calcination in air. Since the organic template molecules (TPAOH in this work) were already removed, the re-dispersed Pt species may occupy several possible positions, including the straight channels, sinusoidal channels and the intersectional crossing. Since the majority of Pt species are located in the sinusoidal channels in the as-synthesized K-PtSn@MFI-560air sample (obtained after calcination in air at 560 ºC) and the amount of migrated Pt species is not high in terms of the total Pt in the whole sample, the Pt species in the sinusoidal channel are still a dominant part in the K-PtSn@MFI-650air, as confirmed by HAADF-iDPC images (see **Fig. S43**). Therefore, when the K-PtSn@MFI-650air sample is reduced by H_2, the Pt clusters formed in the sinusoidal channels can work as the nucleation sites and some of the Pt atoms in the intersectional crossing and the straight channel may migrate to the Pt clusters in the sinusoidal channels. As a consequence, subnanometric PtSn clusters are mainly located in the 10MR sinusoidal channels in the K-PtSn@MFI-650-1C sample. However, if the initial K-PtSn@MFI-560air sample, i.e. the K-PtSn@MFI calcined at lower temperature, is directly reduced by H_2 at 650 ºC, a large fraction of the highly dispersed Pt species on the surface or at the subsurface of MFI zeolite crystallites may form nanoparticles and migrate to the external surface, though part of the Pt species also form subnanometric Pt clusters in the sinusoidal channels inside the crystallites (see **Fig. S50**).

Once the bimetallic PtSn clusters are formed in the PtSn@MFI-650-1C sample, one may be interested on the stability of those subnanometric PtSn clusters during high-temperature calcination

treatment. In our previous work, we have shown that, Pt nanoclusters can be completely disintegrated into isolated Pt atoms when the Pt nanoclusters are trapped in high-silica CHA-type zeolite. To address that issue, the K-PtSn@MFI-650-1C sample has been subjected to another calcination in air at 650 ºC, and the location of Pt species has been studied by the STEM-iDPC imaging technique. As shown in **Fig. 7** and **Fig. S51**, some residual subnanometric Pt clusters can be observed in the STEM images, though the number of Pt clusters observed is much lower than that in the PtSn@MFI-650-1C sample. The paired HAADF-STEM and iDPC images indicate that, both isolated Pt atoms and Pt clusters can be observed in the sinusoidal 10MR channels (**Fig. S52**). These results indicate that, the disintegration of PtSn clusters confined in the sinusoidal 10MR channels did occur during calcination in air at 650 ºC, but the PtSn clusters were not completely transformed into isolated Pt atoms. It is known that, when metallic Pt particles are oxidized, their contrast in the TEM images can decrease [34,35]. Since we are able to observe some Pt clusters remaining in the sinusoidal channels, one plausible scenario that occurs during the high-temperature calcination treatment is the partial disintegration of PtSn clusters. The oxidized Pt and Sn species are slightly redispersed, but still remain in the sinusoidal 10MR channels, instead of migrating across the intersectional voids or 10MR straight channels in the zeolite crystallites.

To confirm that hypothesis, the K-PtSn@MFI-650-1.5C sample has been reduced again by H_2 at 650 ºC, which leads to the formation of the K-PtSn@MFI-650-2C sample. As shown in **Fig. 8**, uniformly distributed subnanometric PtSn clusters are observed again in the MFI zeolite crystallites, even after two cycles of redox treatment at 650 ºC, confirming their superior stability. More importantly, the position of the Pt clusters has also been determined by HAADF-iDPC images, and according to those images, the vast majority of the subnanometric Pt clusters remain located in the 10MR sinusoidal channels (see **Fig. S53-S56**). These results confirm that, the migration of Pt species across the intersectional void and 10MR straight channels during high-temperature calcination in air is not observed within the MFI zeolite crystallites. During the calcination in air, bimetallic PtSn clusters can probably transform into PtOx and SnOx species, as observed with Pt-based nanoparticles in oxidative atmosphere [36-38]. The resultant SnOx species remain in the sinusoidal channels due to the strong interaction with the zeolite framework, and the high affinity between PtOx and SnOx species contribute to the stabilization of Pt species in the sinusoidal channels. The high stability of

subnanometric Pt species can also be reflected in the structural characterizations on the K-PtSn@MFI-650-3C sample. After three cycles of oxidation-reduction treatment at 650 ºC, a large population of subnanometric PtSn clusters with very good dispersion are preserved in the sinusoidal 10MR channels, as revealed by the STEM-iDPC images (**Fig. S57-S61**).

Besides, we have employed in situ CO-IR spectroscopy to study the dispersion of Pt species in MFI zeolites. According to **Fig. S62**, various CO bands adsorbed on Pt nanoparticles and clusters can be observed in the spectra. Notably, after three cycles of redox treatments at 650 ºC, the intensity of CO bands adsorbed on Pt nanoparticles decreases while the band intensity associated with Pt clusters increases in comparison with the K-PtSn@MFI sample prior to high-temperature treatments [39,40]. Furthermore, the band at ~1890 cm^{-1}, which could be related to CO adsorbed on Pt-SnOx interface, decreases after redox treatment, implying a promotion reduction of SnOx species and formation of bimetallic PtSn clusters [41]. These results are consistent with the observation by electron microscopy, further confirming the dispersion of Pt nanoparticles into subnanometric Pt clusters in the K-PtSn@MFI-650-3C sample.

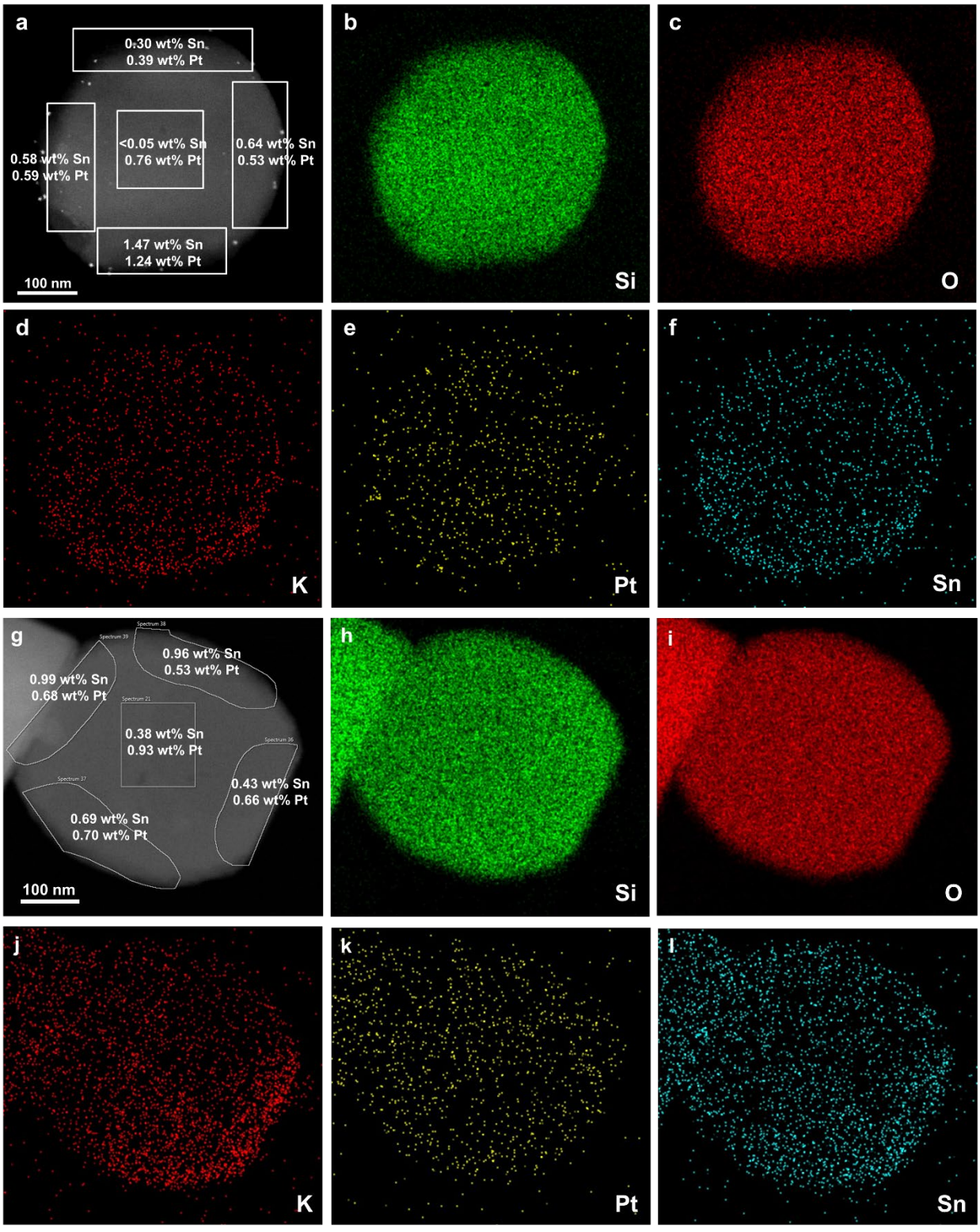

Fig. 9. Distribution of different elements in K-PtSn@MFI-560air and K-PtSn@MFI-650-3C samples measured by STEM-EDS mapping. (a) STEM-HAADF image of a single MFI zeolite crystallite of K-PtSn@MFI-560air sample and (b-f) the spatial distribution of various elements. (g) STEM-HAADF image of a single MFI zeolite crystallite of K-PtSn@MFI-650-3C sample and (h-l) the spatial distribution of various elements. The amount of Sn and Pt in the surface and core regions of the zeolite crystallites are indicated in (a) and (g).

In conventional supported catalysts consisting of Pt-based nanoparticles, both Pt and the second component (such as Fe, Ni or Sn) may show structural transformation when the external environment is changed [42-44]. In the above discussion, we have focused on the location of subnanometric Pt species during the redox treatments based on the atomic-level structural characterization results. The identification of the location of Sn species in MFI zeolite is quite difficult due to their low contrast in STEM images. However, considering the formation of bimetallic PtSn clusters during reduction treatment at 650 ºC, migration of Sn species within the MFI zeolite crystallite may occur in the K-PtSn@MFI sample. We have measured the distribution of Sn species in the MFI zeolite by STEM-EDS mapping and the results indicate that Sn species are enriched at the surface regions of the MFI zeolite crystallites in the pristine K-PtSn@MFI-560air sample, as shown in **Fig. 9a-f** and **Fig. S63**. The surface enrichment of Sn species has also been found with the Sn-MFI materials prepared by one-pot hydrothermal synthesis in the literature [45]. In contrast, the distribution of Pt seems to be more homogeneous than Sn, though some difference can still be observed among different areas in a single zeolite crystallite. Furthermore, a higher calcination treatment at 650 ºC doesn't have influence on the spatial distribution of Sn species (see **Fig. S64**), which should be related to the high stability of Sn(IV) species bonded to the zeolite framework. However, after reduction treatment in H_2 at 650 ºC, the amount of Sn in the core region of the MFI zeolite crystallite increases (see **Fig. 9g-l and Fig. S65**), as observed in others samples after high-temperature reduction treatment, including K-PtSn@MFI-650H_2 (**Fig. S66**) and K-PtSn@MFI-650-1C (**Fig. S67**). During the high-temperature reduction treatment, the Pt clusters located in the core region of the zeolite crystallite can serve as the anchoring sites for the mobile Sn species [46], which migrate from the surface to the core region and form PtSn bimetallic clusters in the sinusoidal channels, resulting in the increase of Sn content in the core region.

The change of spatial distribution of Pt and Sn elements in the K-PtSn@MFI sample has been studied by XPS, which is an averaged analysis technique as a complementary tool to STEM-EDS. The ratio of Sn/Pt in the surface region is 4.8 in the K-PtSn@MFI-650air sample, which is much higher than the Sn/Pt ratio (~0.7) in the whole sample measured by ICP analysis. After H_2 reduction treatment at 650 ºC, the surface Sn/Pt ratio decreases to 2.0, inferring to the migration of Sn from surface to internal space of the zeolite crystallites, being consistent with the STEM-EDS results.

We have carried out the same redox treatment with the K-Pt@MFI sample (with ~1.4 wt% Pt) to

clarify the critical role of Sn species on stabilization of subnanometric Pt clusters during high-temperature redox treatments. After one cycle of treatment at 650 ºC, most of the Pt species exist as small Pt nanoparticles ~1 nm though a small fraction of Pt clusters can also be observed. Due to the growth of the particle size, those Pt particles in the K-Pt@MFI-650-1C sample are no longer confined in the 10MR sinusoidal channels but migrate to the intersectional voids (see **Fig. S68-S69**).

Combining the above results on studying the evolution behavior of subnanometric Pt and Sn species in MFI zeolite crystallites during high-temperature redox treatments, we can achieve a global understanding on how the distribution of the two metal components can be regulated by post-synthesis treatments (as summarized in **Fig. 6**) and these insights lead us to obtain a K-PtSn@MFI sample containing a large population of subnanometric PtSn clusters with very good distribution in the 10MR sinusoidal channels.

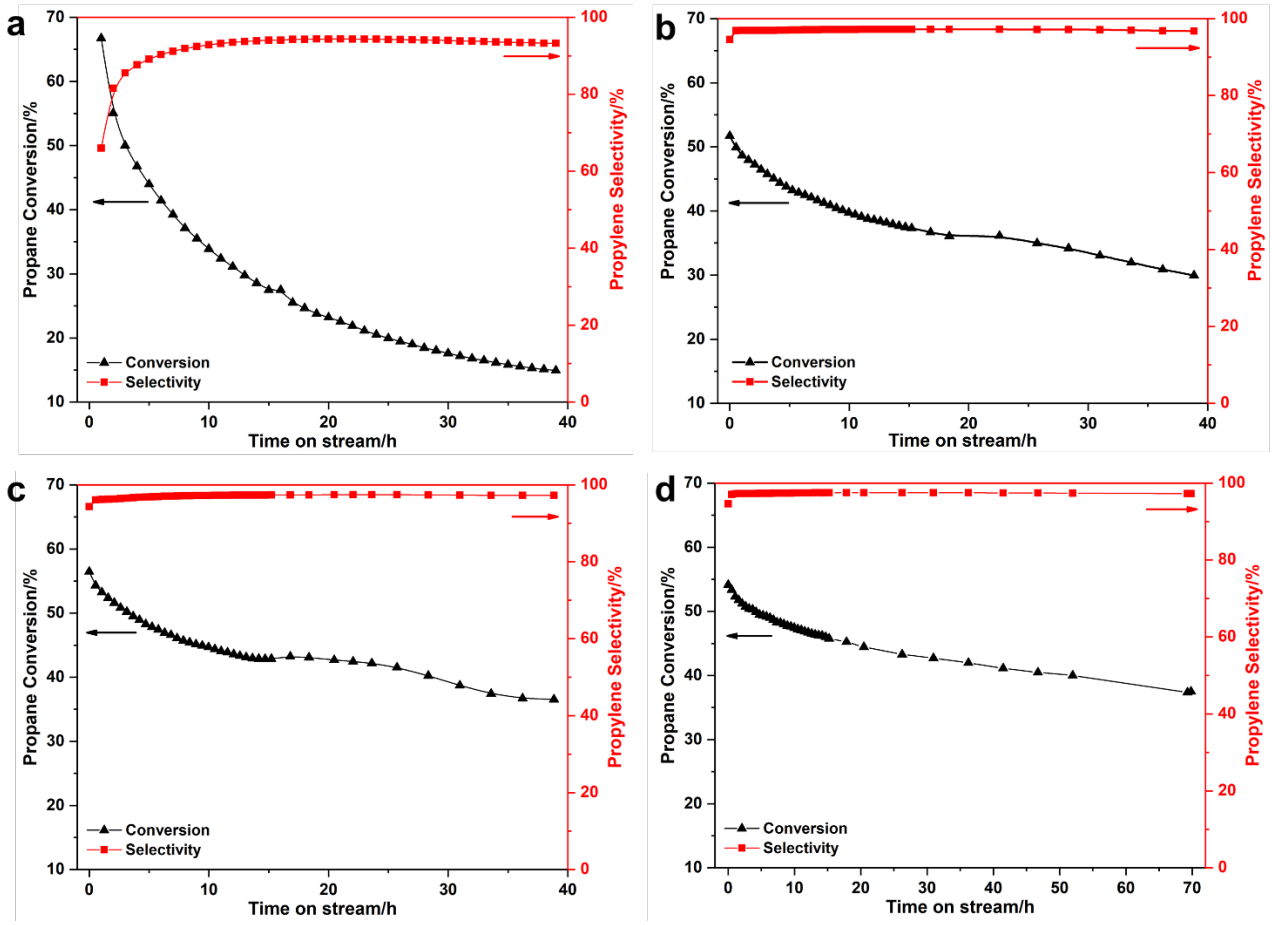

Fig. 10. Catalytic performance of K-PtSn@MFI samples tested under high weight-hour space velocity conditions. Reaction conditions: 20 mg solid catalyst, 5 mL/min of propane and 16 mL/min of N_2 as feed gas, 600 ºC. All the samples were reduced by H_2 in the fix-bed reactor at 600 ºC for 1 h before

the catalytic test. (a) K-PtSn@MFI-560air sample, (b) K-PtSn@MFI-650H_2 sample after reduction by H_2 at 650 ºC for 3 h, (c) K-PtSn@MFI-650-1C sample obtained after one cycle of oxidation-reduction treatment at 650 ºC and (d) K-PtSn@MFI-650-3C sample after three cycles of oxidation-reduction treatment at 650 ºC.

To study the influence of high-temperature redox treatment on the catalytic performance of K-PtSn@MFI sample, we have tested them for propane dehydrogenation. In order to better distinguish different samples, the catalytic tests were carried out at a higher weight-hour space velocity by using less solid catalyst (see **Experimental section** for details). As shown in **Fig. 10a**, if the as-prepared K-PtSn@MFI sample (K-PtSn@MFI-560air) was directly reduced by H_2 in the reactor at 600 ºC for 1 h before the catalytic test, a low initial selectivity to propylene and a fast deactivation can be observed. However, if the same catalyst was reduced by H_2 at 650 ºC for 3 h, a higher initial selectivity to propylene and much slower deactivation was obtained, which can be ascribed to the formation of more bimetallic PtSn species after high-temperature reduction treatment. If the sample was treated with one cycle of calcination-reduction at 650 ºC, the deactivation can be further slowed down. Remarkably, after three cycles of redox treatment, the K-PtSn@MFI-650-3C sample presents further improved catalytic performance compared to the K-PtSn@MFI-650-1C and K-PtSn@MFI-650-2C sample (see **Fig. S70**). The marked decrease of deactivation rate observed with the samples after high-temperature redox treatments can be ascribed to the formation of bimetallic PtSn clusters, in which the atomically Sn species are bonded to the surface of subnanometric Pt clusters confined in the 10MR channels, as revealed by our recent work [47].

If the high-temperature redox treatment is directly carried out with the as-synthesized K-PtSn@MFI sample, the resultant K-PtSn@MFI-650air-direct sample contains a higher population of Pt nanoparticles on the external surface of MFI zeolite crystallites, though subnanometric Pt clusters are also observed inside the zeolite crystallites (see **Fig. S71-S74**). Considering that the removal of organic structure-directing agent in the as-synthesized zeolite materials is exothermic, the local temperature within the metal-zeolite materials could be very high if the calcination is performed at high temperature. The disadvantage of direct redox treatment is also reflected in the catalytic performance for propane dehydrogenation. As shown in **Fig. S75**, the K-PtSn@MFI-650air-direct sample prepared by direct

calcination at 650 ºC in air shows a lower initial conversion of propane and a slightly faster deactivation rate compared to the K-PtSn@MFI-650-1C sample.

After the catalytic tests, the K-PtSn@MFI materials have been characterized by electron microscopy. Basically, the morphology of the catalyst and the size distribution of Pt particles are similar to the fresh catalysts according to the STEM-HAADF images shown in **Fig. S76 to Fig. S81**. Particularly, in the case of the K-PtSn@MFI-65-3C, which gives the best catalytic performance, the uniform distribution of Pt clusters inside the MFI zeolite crystallites is preserved after ~70 h of propane dehydrogenation reaction (see **Fig. S82-S83**). And the location of Pt clusters in the 10MR sinusoidal channels is also confirmed by the paired HAADF-STEM and iDPC images (**Fig. S84**).

Nevertheless, we have also compared the PtSn@MFI-650-3C sample with the K-PtSn@MFI sample with a lower Pt loading (~0.4 wt% of Pt, named as K-PtSn@MFI-lessPt) reported in our previous work [31], in which Pt mainly exists as subnanometric Pt clusters in the sinusoidal channels. In terms of the initial turnover frequency (TOF) for propane dehydrogenation reaction, the K-PtSn@MFI-650-3C sample is ca. 70% of the activity of the as-synthesized K-PtSn@MFI-lessPt sample (see **Fig. S85**). Considering the Pt loading in PtSn@MFI-650-3C is ~3 times of that for the K-PtSn@MFI-lessPt, a higher propylene yield can be obtained with PtSn@MFI-650-3C when using the same amount of solid catalyst. Indeed, after the same high-temperature redox treatments at 650 ºC with the K-PtSn@MFI-lessPt sample, the K-PtSn@MFI with high Pt loading is clearly more active than the K-PtSn@MFI with low Pt loading (K-PtSn@MFI-lessPt-650-3C), when using the same amount of solid catalyst (see **Fig. S86**). The above results clearly indicate that high-temperature redox treatment can be an effective method for the generation of high-density of subnanometric Pt clusters confined in zeolites, which is of interest for practical applications.

4. Conclusions

In the work, we have presented the regioselective encapsulation of subnanometric Pt clusters in the sinusoidal channels of MFI zeolite by one-pot synthesis with a relatively high Pt loading (~1.4 wt%). Furthermore, we have described at atomic level the structural evolution of subnanometric Pt and Sn species during high-temperature redox treatments. In particular we have evidenced that the Pt particles on the external surface in the as-synthesized material can disintegrate into subnanometric Pt species

and get stabilized in the zeolite channels, mostly as isolated Pt atoms after high-temperature calcination in air. While a large fraction of the Sn species remains on the surface region of the MFI zeolite crystallites after calcination in air. During the subsequent high-temperature reduction treatment, part of the Sn species can migrate from the surface to the internal region where they interact with the subnanometric Pt clusters formed from the isolated Pt atoms, leading to the formation of dense subnanometric PtSn clusters with high regioselectivity in the sinusoidal 10MR channels and excellent catalytic performance for propane dehydrogenation.

Appendix A. Supplementary material

Supporting Information Available: Materials and Experimental Methods including the additional characterization and catalytic results, supplementary discussion and references.

Acknowledgement

This work has been supported by the European Union through the European Research Council (grant ERC-AdG-2014-671093, SynCatMatch) and the Spanish government through the "Severo Ochoa Program" (SEV-2016-0683). The authors also thank Microscopy Service of UPV for the TEM and STEM measurements. The XAS measurements were carried out in CLAESS beamline of ALBA synchrotron and BM23 beamline at ESRF synchrotron. The kind supports from the scientific staffs in ALBA and ESRF are greatly appreciated. High-resolution STEM measurements were performed at DME-UCA node of ELECMI in Cadiz University, with financial support from FEDER/MINECO (MAT2017-87579-R and MAT2016-81118-P). C.W.L. thanks CAPES (Science without Frontiers Process no. 13191/13-6) for a predoctoral fellowship. Financial support on this work from ExxonMobil is greatly acknowledged.

References

[1] B.C. Gates, Supported Metal Clusters: Synthesis, Structure, and Catalysis, Chem. Rev. 95 (1995) 511-522.
[2] M. Flytzani-Stephanopoulos, B.C. Gates, Atomically Dispersed Supported Metal Catalysts, Annu. Rev. Chem. Biomol. Eng. 3 (2012) 545-574.
[3] L. Liu, A. Corma, Metal Catalysts for Heterogeneous Catalysis: From Single Atoms to

Nanoclusters and Nanoparticles, Chem. Rev. 118 (2018) 4981-5079.
[4] A. Wang, J. Li, T. Zhang, Heterogeneous single-atom catalysis, Nat. Rev. Chem. 2 (2018) 65-81.
[5] S. Ji, Y. Chen, X. Wang, Z. Zhang, D. Wang, Y. Li, Chemical Synthesis of Single Atomic Site Catalysts, Chem. Rev. 2020, doi: 10.1021/acs.chemrev.9b00818.
[6] Y. Chen, S. Ji, C. Chen, Q. Peng, D. Wang, Y. Li, Single-Atom Catalysts: Synthetic Strategies and Electrochemical Applications, Joule 2 (2018) 1242-1264.
[7] A. Beniya, S. Higashi, Towards dense single-atom catalysts for future automotive applications, Nat. Catal. 2 (2019) 590-602.
[8] R. Lang, W. Xi, J.C. Liu, Y.T. Cui, T. Li, A.F. Lee, F. Chen, Y. Chen, L. Li, L. Li, J. Lin, S. Miao, X. Liu, A.Q. Wang, X. Wang, J. Luo, B. Qiao, J. Li, T. Zhang, Non defect-stabilized thermally stable single-atom catalyst, Nat. Commun. 10 (2019) 234.
[9] D. Kunwar, S. Zhou, A. DeLaRiva, E.J. Peterson, H. Xiong, X.I. Pereira-Hernández, S.C. Purdy, R. ter Veen, H.H. Brongersma, J.T. Miller, H. Hashiguchi, L. Kovarik, S. Lin, H. Guo, Y. Wang, A.K. Datye, Stabilizing High Metal Loadings of Thermally Stable Platinum Single Atoms on an Industrial Catalyst Support, ACS Catal. 9 (2019) 3978-3990.
[10] X.I. Pereira-Hernandez, A. DeLaRiva, V. Muravev, D. Kunwar, H. Xiong, B. Sudduth, M. Engelhard, L. Kovarik, E.J.M. Hensen, Y. Wang, A.K. Datye, Tuning Pt-CeO_2 interactions by high-temperature vapor-phase synthesis for improved reducibility of lattice oxygen, Nat. Commun. 10 (2019) 1358.
[11] Y. Ren, Y. Tang, L. Zhang, X. Liu, L. Li, S. Miao, D. Sheng Su, A. Wang, J. Li, T. Zhang, Unraveling the coordination structure-performance relationship in Pt_1/Fe_2O_3 single-atom catalyst, Nat. Commun. 10 (2019) 4500.
[12] N. Kosinov, C. Liu, E.J.M. Hensen, E.A. Pidko, Engineering of Transition Metal Catalysts Confined in Zeolites, Chem. Mater. 30 (2018) 3177-3198.
[13] N. Wang, Q. Sun, J. Yu, Ultrasmall Metal Nanoparticles Confined within Crystalline Nanoporous Materials: A Fascinating Class of Nanocatalysts, Adv. Mater. 31 (2019) e1803966.
[14] S.M. Wu, X.Y. Yang, C. Janiak, Confinement Effects in Zeolite-Confined Noble Metals, Angew. Chem. Int. Ed. 58 (2019) 12340-12354.
[15] M. Moliner, J.E. Gabay, C.E. Kliewer, R.T. Carr, J. Guzman, G.L. Casty, P. Serna, A. Corma, Reversible Transformation of Pt Nanoparticles into Single Atoms inside High-Silica Chabazite Zeolite, J. Am. Chem. Soc. 138 (2016) 15743-15750.
[16] Q. Sun, N. Wang, Q. Fan, L. Zeng, A. Mayoral, S. Miao, R. Yang, Z. Jiang, W. Zhou, J. Zhang, T. Zhang, J. Xu, P. Zhang, J. Cheng, D.C. Yang, R. Jia, L. Li, Q. Zhang, Y. Wang, O. Terasaki, J. Yu, Subnanometer Bimetallic Pt-Zn Clusters in Zeolites for Propane Dehydrogenation, Angew. Chem. Int. Ed. (2020), doi: 10.1002/anie.202003349
[17] M. Moliner, J. Gabay, C. Kliewer, P. Serna, A. Corma, Trapping of Metal Atoms and Metal Clusters by Chabazite under Severe Redox Stress, ACS Catal. 8 (2018), 9520-9528.
[18] S. Goel, S. I. Zones, E. Iglesia, Encapsulation of Metal Clusters within MFI via Interzeolite Transformations and Direct Hydrothermal Syntheses and Catalytic Consequences of their Confinement, J. Am. Chem. Soc., 136 (2014) 15280-15290.
[19] N. Wang, Q. Sun, R. Bai, X. Li, G. Guo, J. Yu, In Situ Confinement of Ultrasmall Pd Clusters within Nanosized Silicalite-1 Zeolite for Highly Efficient Catalysis of Hydrogen Generation, J. Am. Chem. Soc., 138 (2016) 7484-7487.
[20] J. Zhang, L. Wang, B. Zhang, H. Zhao, U. Kolb, Y. Zhu, L. Liu, Y. Han, G. Wang, C. Wang, D.S.

Su, B.C. Gates, F.-S. Xiao, Sinter-resistant metal nanoparticle catalysts achieved by immobilization within zeolite crystals via seed-directed growth, Nat. Catal. 1 (2018) 540-546.
[21] K.F. Kalz, R. Kraehnert, M. Dvoyashkin, R. Dittmeyer, R. Glaser, U. Krewer, K. Reuter, J.D. Grunwaldt, Future Challenges in Heterogeneous Catalysis: Understanding Catalysts under Dynamic Reaction Conditions, ChemCatChem 9 (2017) 17-29.
[22] M.A. Newton, Dynamic adsorbate/reaction induced structural change of supported metal nanoparticles: heterogeneous catalysis and beyond, Chem. Soc. Rev. 37 (2008) 2644-2657.
[23] L. Liu, D.M. Meira, R. Arenal, P. Concepcion, A.V. Puga, A. Corma, Determination of the Evolution of Heterogeneous Single Metal Atoms and Nanoclusters under Reaction Conditions: Which Are the Working Catalytic Sites? ACS Catal. 9 (2019) 10626-10639.
[24] E. Borfecchia, P. Beato, S. Svelle, U. Olsbye, C. Lamberti, S. Bordiga, Cu-CHA - a model system for applied selective redox catalysis, Chem. Soc. Rev. 47 (2018) 8097-8133.
[25] L. Liu, D.N. Zakharov, R. Arenal, P. Concepcion, E.A. Stach, A. Corma, Evolution and stabilization of subnanometric metal species in confined space by in situ TEM, Nat. Commun. 9 (2018) 574.
[26] B.C. Gates, Atomically Dispersed Supported Metal Catalysts: Seeing Is Believing. Trends Chem. 1 (2019) 99-110.
[27] M. López-Haro, M. Tinoco, S. Fernández-Garcia, X. Chen, A.B. Hungria, M.Á. Cauqui, J.J. Calvino, A Macroscopically Relevant 3D-Metrology Approach for Nanocatalysis Research, Particle Particle Systems Characterization, 35 (2018) 1700343.
[28] L. Simonelli, C. Marini, W. Olszewski, M. Avila Perez, N. Ramanan, G. Guilera, V. Cuartero, K. Klementiev, N. L. Saini, CLÆSS: The hard X-ray absorption beamline of the ALBA CELLS synchrotron. Cogent Physics 3 (2016) 1231987.
[29] O. Mathon, A. Beteva, J. Borrel, D. Bugnazet, S. Gatla, R. Hino, I. Kantor, T. Mairs, M. Munoz, S. Pasternak, F. Perrin, S. Pascarelli, The time-resolved and extreme conditions XAS (TEXAS) facility at the European Synchrotron Radiation Facility: the general-purpose EXAFS bending-magnet beamline BM23, J Synchrotron Radiat. 22 (2015) 1548-1554.
[30] B. Ravel, M. Newville, ATHENA, ARTEMIS, HEPHAESTUS: data analysis for X-ray absorption spectroscopy using IFEFFIT. J. Synchrotron Radiat. 12 (2005) 537-541.
[31] L. Liu, M. Lopez-Haro, C.W. Lopes, C. Li, P. Concepcion, L. Simonelli, J.J. Calvino, A. Corma, Regioselective generation and reactivity control of subnanometric platinum clusters in zeolites for high-temperature catalysis, Nat. Mater. 18 (2019) 866-873.
[32] K. Morgan, A. Goguet, C. Hardacre, Metal Redispersion Strategies for Recycling of Supported Metal Catalysts: A Perspective, ACS Catal. 5 (2015) 3430-3445.
[33] J. Jones, H. Xiong, A.T. DeLaRiva, E.J. Peterson, H. Pham, S.R. Challa, G. Qi, S. Oh, M.H. Wiebenga, X.I. Pereira Hernandez, Y. Wang, A.K. Datye, Thermally stable single-atom platinum-on-ceria catalysts via atom trapping, Science 353 (2016) 150-154.
[34] F. Behafarid, S. Pandey, R.E. Diaz, E.A. Stach, B.R. Cuenya, An in situ transmission electron microscopy study of sintering and redispersion phenomena over size-selected metal nanoparticles: environmental effects, Phys. Chem. Chem. Phys. 16 (2014) 18176-18184.
[35] E.A. Derevyannikova, T.Y. Kardash, A.I. Stadnichenko, O.A. Stonkus, E.M. Slavinskaya, V.A. Svetlichnyi, A.I. Boronin, Structural Insight into Strong Pt–CeO2 Interaction: From Single Pt Atoms to PtOx Clusters, J. Phys. Chem. C 123 (2018) 1320-1334.
[36] Y. Uemura, Y. Inada, K.K. Bando, T. Sasaki, N. Kamiuchi, K. Eguchi, A. Yagishita, M. Nomura,

M. Tada, Y. Iwasawa, In situ time-resolved XAFS study on the structural transformation and phase separation of Pt_3Sn and PtSn alloy nanoparticles on carbon in the oxidation process, Phys. Chem. Chem. Phys. 13 (2011) 15833-15844.

[37] A. Moscu, C. Theodoridi, L. Cardenas, C. Thieuleux, D. Motta-Meira, G. Agostini, Y. Schuurman, F. Meunier, CO dissociation on Pt-Sn nanoparticles triggers Sn oxidation and alloy segregation, J. Catal. 359 (2018) 76-81.

[38] W.D. Michalak, J.M. Krier, S. Alayoglu, J.-Y. Shin, K. An, K. Komvopoulos, Z. Liu, G.A. Somorjai, CO oxidation on PtSn nanoparticle catalysts occurs at the interface of Pt and Sn oxide domains formed under reaction conditions, J. Catal. 312 (2014) 17-25.

[39] P. Concepcion, Y. Perez, J.C. Hernandez-Garrido, M. Fajardo, J.J. Calvino, A. Corma, The promotional effect of Sn-beta zeolites on platinum for the selective hydrogenation of alpha,beta-unsaturated aldehydes, Phys. Chem. Chem. Phys. 15 (2013) 12048-12055.

[40] A.I. Serykh, O.P. Tkachenko, V. Yu. Borovkov, V.B. Kazansky, M. Beneke, N.I. Jaeger, G. Schulz-Ekloff, Stable subnanometre Pt clusters in zeolite NaX via stoichiometric carbonyl complexes: Probing of negative charge by DRIFT spectroscopy of adsorbed CO and H_2, Physical Chemistry Chemical Physics, 2 (2000) 5647-5652.

[41] L.-C. de Menorval, A. Chaqroune, B.Coq, F. Figueras, Characterization of mono- and bi-metallic platinum catalysts using CO FTIR spectroscopy Size effects and topological segregation, J. Chem. Soc., Faraday Trans. 93 (1997) 3715-3720.

[42] S.F. Tan, S.W. Chee, Z. Baraissov, H. Jin, T.L. Tan, U. Mirsaidov, Real-Time Imaging of Nanoscale Redox Reactions over Bimetallic Nanoparticles, Adv. Funct. Mater. 29 (2019) 1903242.

[43] S. Prabhudev, M. Bugnet, G.Z. Zhu, C. Bock, G.A. Botton, Surface Segregation of Fe in Pt-Fe Alloy Nanoparticles: Its Precedence and Effect on the Ordered-Phase Evolution during Thermal Annealing, ChemCatChem 7 (2015) 3655-3664.

[44] B.-W. Zhang, H.-L. Yang, Y.-X. Wang, S.-X. Dou, H.-K. Liu, A Comprehensive Review on Controlling Surface Composition of Pt-Based Bimetallic Electrocatalysts, Adv. Energy Mater. 8 (2018) 1703597.

[45] G.M. Lari, P.Y. Dapsens, D. Scholz, S. Mitchell, C. Mondelli, J. Pérez-Ramírez, Deactivation mechanisms of tin-zeolites in biomass conversions, Green Chem. 18 (2016) 1249-1260.

[46] G. Wang, H. Zhang, H. Wang, Q. Zhu, C. Li, H. Shan, The role of metallic Sn species in catalytic dehydrogenation of propane: Active component rather than only promoter, J. Catal., 344 (2016) 606-608.

[47] L. Liu, M. Lopez-Haro, C.W. Lopes, S. Rojas-Buzo, P. Concepcion, R. Manzorro, L. Simonelli, A. Sattler, P. Serna, J.J. Calvino, A. Corma, Structural modulation and direct measurement of subnanometric bimetallic PtSn clusters confined in zeolites, Nat. Catal., 2020, doi: 10.1038/s41929-020-0472-7.